






Spin excitations in the frustrated triangular lattice antiferromagnet NaYbO₂

Mitchell M. Bordelon ¹, Chunxiao Liu ², Lorenzo Posthuma,¹ P. M. Sarte,³ N. P. Butch,⁴ Daniel M. Pajerowski ⁵, Arnab Banerjee,⁵ Leon Balents ⁶ and Stephen D. Wilson ^{1,*}

¹Materials Department, University of California, Santa Barbara, California 93106, USA

²Department of Physics, University of California, Santa Barbara, California 93106, USA

³California Nanosystems Institute, University of California, Santa Barbara, California 93106, USA

⁴NIST Center for Neutron Research, National Institute of Standards and Technology, Gaithersburg, Maryland 20899, USA

⁵Neutron Scattering Division, Oak Ridge National Laboratory, Oak Ridge, Tennessee 37831, USA

⁶Kavli Institute for Theoretical Physics, University of California, Santa Barbara, California 93106, USA



(Received 10 March 2020; revised manuscript received 20 May 2020; accepted 28 May 2020; published 22 June 2020)

Here we present a neutron scattering-based study of magnetic excitations and magnetic order in NaYbO₂ under the application of an external magnetic field. The crystalline electric field-split $J = 7/2$ multiplet structure is determined, revealing a mixed $|m_z\rangle$ ground-state doublet, and is consistent with a recent report by Ding *et al.* [L. Ding, P. Manuel, S. Bachus, F. Grubler, P. Gegenwart, J. Singleton, R. D. Johnson, H. C. Walker, D. T. Adroja, A. D. Hillier, and A. A. Tsirlin, *Phys. Rev. B* **100**, 144432 (2019)]. Our measurements further suggest signatures of exchange effects in the crystal-field spectrum, manifested by a small splitting in energy of the transition into the first excited doublet. The field dependence of the low-energy magnetic excitations across the transition from the quantum disordered ground state into the fluctuation-driven ordered regime is analyzed. Signs of a first-order phase transition into a noncollinear ordered state are revealed at the upper-field phase boundary of the ordered regime, and higher-order magnon scattering, suggestive of strong magnon-magnon interactions, is resolved within the previously reported up-up-down phase. Our results reveal a complex phase diagram of field-induced order and spin excitations within NaYbO₂ and demonstrate the dominant role of quantum fluctuations across a broad range of fields within its interlayer frustrated triangular lattice.

DOI: [10.1103/PhysRevB.101.224427](https://doi.org/10.1103/PhysRevB.101.224427)

I. INTRODUCTION

The triangular lattice antiferromagnet is a long-studied archetype of geometrically driven magnetic frustration. It has been widely explored both experimentally and theoretically with goals to realize unconventional ground states that may arise from tailoring the degree of frustration, underlying anisotropies, and quantum fluctuations inherent to the moments decorating the magnetic lattice [1–8]. While in the ideal Heisenberg limit both classical and quantum moments develop three-sublattice 120° order [9,10], perturbing away from this limit realizes a rich phase space. In particular, the search for conditions that realize ground states disordered by quantum fluctuations remains of sustained interest, with proposed phases ranging from “resonating valence bond” states [1,2,11], to quantum dimer phases [12–14], to a variety of spin liquid phases [15–23], some of which may realize long-range entanglement. However, finding pristine material systems to match many of these models remains an outstanding challenge, as effects in real materials such as orbital ordering [24–26], Jahn-Teller distortions [27,28], anisotropic exchange [29–32], and exchange disorder [33–36] can either induce order, quench the moments entirely, or reduce the dimensionality to quasi-one-dimensional.

Studies of several classes of rare-earth oxides have recently shown that model planes of equilateral triangles of $4f$ moments form in a high-symmetry setting ideal for studying quantum fluctuations within this system. Rare-earth lanthanides with the YbFe₂O₄ structure type (YbMgGaO₄ [15,37–44] and TmMgGaO₄ [45–47]) realize a spin Hamiltonian with spin-orbit entangled Ln³⁺ moments (Ln=lanthanide) and anisotropic exchange couplings. At low temperatures, quantum spin liquid (QSL) states have been proposed [15,48], and experiments suggest the absence of long-range magnetic order in select compounds. The archetypal material in this class is YbMgGaO₄, originally proposed as a QSL candidate due to its lack of long-range magnetic order and the observation of a low-temperature continuum of magnetic excitations; however, the influence of innate chemical disorder within its lattice complicates this interpretation.

Disorder in YbMgGaO₄ arises from two equally intermixed Mg²⁺:Ga³⁺ layers that reside between the trivalent Yb-ion triangular sheets. This alters the local chemical environment about the YbO₆ octahedra and introduces exchange disorder, and some recent studies have suggested the formation of a weakly bound spin-glass ground state that freezes at low temperatures [36,49]. However, competing interpretations of YbMgGaO₄ have also proposed that the chemical disorder may enhance quantum fluctuations in favor of a spin liquid state [50]. Other experiments failed to resolve a true spin freezing in this system [51,52] and are instead consistent with

*stephendwilson@ucsb.edu

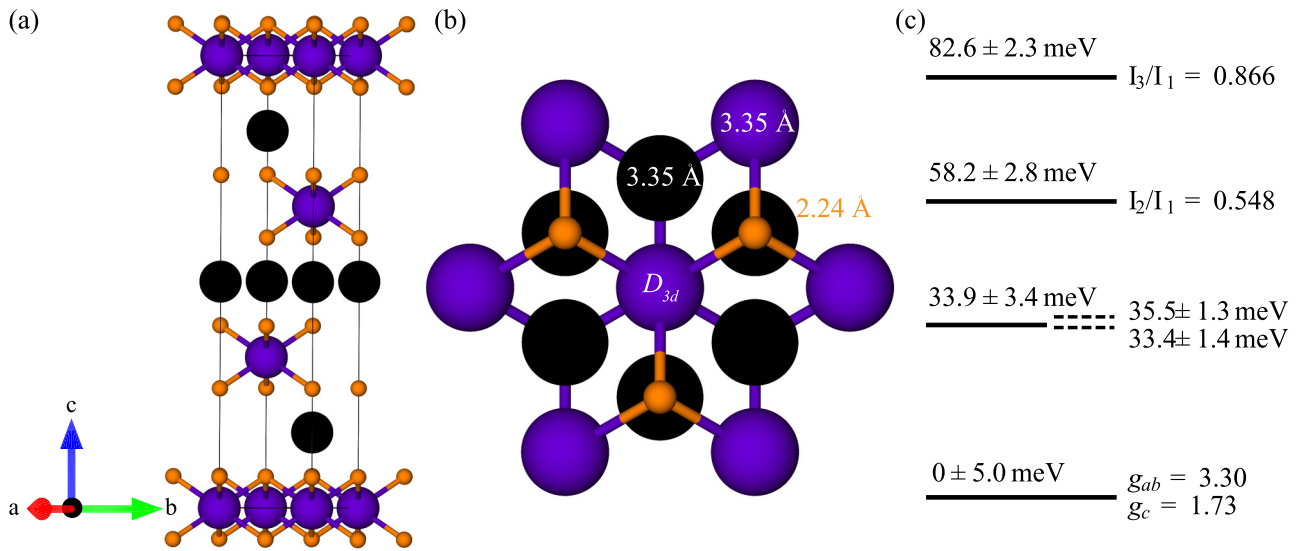


FIG. 1. (a) The NaYbO₂ structure ($R\bar{3}m$, 1.6 K [54]) contains alternating layers of equilateral triangular YbO₆ octahedra (Yb, purple; O, orange) and Na ions (black). (b) Top-down view of the local Yb³⁺ D_{3D} environment extended to two coordination shells. From the central Yb ion, six O²⁻, six Na⁺, and six Yb³⁺ ions reside at 2.24, 3.35, and 3.35 Å, respectively. (c) In the D_{3D} environment, Yb creates four Kramer doublets as observed from crystalline electric field (CEF) fits to inelastic neutron-scattering data. Listed errors correspond to instrumental resolutions at $E_i = 150$ meV (solid lines) and $E_i = 60$ meV (dashed lines). The ground state has anisotropic g factors of $g_c = 1.73$ and $g_{ab} = 3.30$ [54]. Dashed lines next to the first excited CEF doublet represent experimentally observed splitting due to exchange-induced CEF dispersions observed in $E_i = 60$ meV data. Intensity ratios of the second and third excitations (I_2/I_1 , I_3/I_1) were obtained relative to the first CEF state. Uncertainties specified next to energy values are the calculated instrument energy resolution at those energies.

persistent fluctuating valence bonds at the lowest temperatures measured. While the exact nature of its magnetism remains in dispute, studies of YbMgGaO₄ and related variants in the YbFe₂O₄ materials family have provided a clear rationale behind searching for quantum disorder in strongly spin-orbit coupled $J_{\text{eff}} = 1/2$ Ln-ion systems on the triangular lattice.

Building from this, an alternate family of the form $ALnX_2$ (A = alkali-metal ion, Ln = lanthanide ion, X = chalcogen anion) has been identified. These compounds are composed of triangular planes populated with trivalent Ln ions, and experiments have reported that select variants host a quantum disordered magnetic ground state [53–63]. The key appeal of members of this family forming in the α -NaFeO₂ structure type is their realization of an ideal triangular lattice of Ln ions absent the interstitial chemical disorder.

Specifically, NaYbO₂ [53,54,56] (Fig. 1) is an intriguing candidate to realize a quantum disordered ground state. NaYbO₂, like YbMgGaO₄, crystallizes in the $R\bar{3}m$ space group and contains equilateral triangular layers composed of trigonally distorted (D_{3D} local point group) YbO₆ octahedra. However, in NaYbO₂, the in-plane Yb-Yb distance is ≈ 3.35 Å at 1.6 K versus ≈ 3.4 Å in YbMgGaO₄ [38–44], resulting in an increased antiferromagnetic exchange field of $\theta_{\text{CW}} = -10.3$ K [54] relative to $\theta_{\text{CW}} = -4$ K in YbMgGaO₄ [38–44].

In NaYbO₂, a single separating layer of Na ions renders the interlayer Yb-Yb distance close enough to be nearly equivalent with the next-nearest-neighbor in-plane distance, making interplanar interactions relevant in low-temperature exchange models [54]. This differentiates NaYbO₂ from YbMgGaO₄ that contains two nonmagnetic cationic layers separating Yb ion sheets at a larger distance. The relevant physical models for NaYbO₂ and YbMgGaO₄ may differ due to this distinc-

tion. In NaYbO₂, the Yb sheets stack in an ABC sequence such that Yb ions within a given plane will project into the center of Yb triangles within neighboring layers such that all interplane Yb ions are equidistant from one another [54]. Three equivalent, antiferromagnetically coupled interplane bonds contribute to three-dimensional (3D) geometrical frustration, bringing the material out of the typically studied regime of purely two-dimensional (2D) triangular lattice antiferromagnets.

Recent work has shown that NaYbO₂ does not magnetically order above 50 mK in zero field and instead manifests a low-energy continuum of spin fluctuations [53,54,56]. These results are suggestive of a native, quantum disordered ground state held by the $J_{\text{eff}} = 1/2$ triangular lattice of Yb³⁺ moments. The ability to push this magnetic lattice into a fluctuation-driven up-up-down antiferromagnetic state under modest magnetic fields ($H \approx 3$ –5 T) makes it a unique platform for exploring the critical phase boundary between fluctuation-driven order and disorder.

In this paper, we explore the evolution of low-energy magnetic excitations across this phase boundary as well as the onset of long-range magnetic order under applied magnetic field. The first part of this paper reviews the single-ion spin excitations associated with the intramultiplet excitations within the Yb³⁺ $J = 7/2$ manifold split by the D_{3D} crystal field. The ground-state doublet determined is largely in agreement with recent studies [53]; however, our data further reveal potential exchange splitting within the crystalline electric-field excitation spectrum. At lower energies, we examine the detailed field dependence of the low-energy continuum of scattering about the $Q = (1/3, 1/3, 0)$ two-dimensional antiferromagnetic ordering zone center.

Our spin-wave calculations qualitatively capture the field evolution of dynamics endemic to the up-up-down phase, and an anomalous band of excitations above the single-magnon cutoff is identified in the ordered state. Upon crossing the high-field phase boundary of the ordered state, we observe the hysteretic onset of long-range order, suggesting the formation of a noncollinear ordered state and the presence of a first-order, high-field phase boundary prior to entering the quantum paramagnetic regime. Our results demonstrate a complex evolution of order under applied field in NaYbO₂ and unconventional spin dynamics both within the low-field quantum disordered regime as well as within the fluctuation-driven up-up-down state.

II. METHODS

A. Sample preparation

Polycrystalline samples of NaYbO₂ were produced via a solid-state reaction of Yb₂O₃ (99.99%, Alfa Aesar) and Na₂CO₃ (99.997%, Alfa Aesar) in a 1:1.25 molar ratio by firing at 1000 °C for three days followed by regrinding and refriring to 1000 °C for 24 h in air. Volatility of Na₂CO₃ during the reaction can be controlled via crucible size and reactant mass. This results in NaYbO₂ with a small excess of Na₂CO₃ (1–5%) that inhibits the reformation of magnetic Yb₂O₃ into samples. Samples were stored in a dry, inert environment, and all measurements were taken with minimal sample exposure to the atmosphere.

B. Neutron scattering

Low-energy inelastic neutron-scattering (INS) data were collected on 8 g of NaYbO₂ powder on the Disc Chopper Spectrometer (DCS) instrument at the National Institute of Standards and Technology (NIST) Center for Neutron Research, NIST, and on the Cold Neutron Chopper Spectrometer (CNCS) instrument at the Spallation Neutron Source, Oak Ridge National Laboratory (ORNL). A 10-T magnet, dilution insert, and incident neutrons with an incident energy $E_i = 3.27$ meV in the medium-resolution chopper setting were used at DCS. A 7-T magnet, dilution insert, and incident neutrons of $E_i = 3.32$ meV were used for experiments at CNCS. Magnet background at CNCS was removed by subtracting scans collected measuring an empty copper can at 1.8 K. High-energy inelastic neutron-scattering data were obtained at the wide Angular-Range Chopper Spectrometer (ARCS) at the Spallation Neutron Source, ORNL. Data were collected on 5 g of NaYbO₂ powder with two incident neutron energies of $E_i = 60$ meV (Fermi 2, Fermi frequency 420 Hz) and 150 meV (Fermi 2, Fermi frequency 600 Hz) at both 300 and 5 K in a top loading cryostat. Background scattering from the aluminum sample can was removed from these data by obtaining data at both energies and temperatures from an empty canister.

Elastic line analyses were conducted on DCS data by integrating $|Q|$ cuts between $E = [-0.1, 0.1]$ meV. In these data, no extra peaks due to Na₂CO₃ and superior $|Q|$ resolution allowed for the determination of magnetic Bragg reflections corresponding to the $\mathbf{q}_1 = (1/3, 1/3, 0)$ and $\mathbf{q}_2 = (0, 0, 0)$ ordering wave vectors previously reported [54]. The

$\mathbf{Q} = (1/3, 1/3, 0)$ and $(1/3, 1/3, 2)$ peaks were tracked as a function of field from 0 to 10 T and from 10 to 0 T by fitting data between $|Q| = [1.2, 1.29]$ and $[1.38, 1.52]$ Å⁻¹, respectively, to Gaussian functions and extracting their integrated intensities.

C. Crystalline electric-field analysis

Following Hund's rules, the $4f^{13}$ Yb³⁺ ions in NaYbO₂ have total angular momentum $J = 7/2$ ($L = 3, S = 1/2$). This eightfold degenerate ($2J + 1 = 8$) Yb ion state is split by the D_{3D} crystalline electric-field (CEF) environment within the material, which, via Kramers theorem, may be maximally split into a series of four doublets. The CEF interaction is dominated by the shell of charges closest to the central Yb ion with diminishing perturbations by shells of charges further away. Therefore, the primary splitting of the Yb³⁺ manifold is due to the O²⁻ ionic shell in the trigonally compressed YbO₆ octahedra followed by the neighboring Yb³⁺ and Na⁺ cationic shells as shown in Fig. 1(b).

To minimize the number of terms in the CEF Hamiltonian, the \hat{z} direction was chosen to align with the highest-symmetry threefold axis. In NaYbO₂, this coincides with the c axis, and the CEF Hamiltonian is written with CEF parameters B_n^m and Steven's operators \hat{O}_n^m [64] as

$$H_{\text{CEF}} = B_2^0 \hat{O}_2^0 + B_4^0 \hat{O}_4^0 + B_4^3 \hat{O}_4^3 + B_6^0 \hat{O}_6^0 + B_6^3 \hat{O}_6^3 + B_6^6 \hat{O}_6^6. \quad (1)$$

This Hamiltonian generates the Coulomb potential created by charges surrounding the central Yb ion in NaYbO₂ and can include multiple ionic shells. Diagonalizing the Hamiltonian returns relative CEF levels E_0, E_1, E_2 , and E_3 and eigenvectors $\phi_0^\pm, \phi_1^\pm, \phi_2^\pm$, and ϕ_3^\pm . The g -tensor components of the ground-state Kramers doublet are calculated with the ground-state wave functions and Landé g factor ($g_J = 8/7$ for Yb³⁺) by

$$g_c = 2g_J |\langle \phi_0^\pm | J_z | \phi_0^\pm \rangle|, \quad (2)$$

$$g_{ab} = g_J |\langle \phi_0^\pm | J_\pm | \phi_0^\mp \rangle|. \quad (3)$$

When $T \ll E_1$, the relative intensity of the i th level from the ground-state doublet is given by

$$\sum_{J_x, J_y, J_z, \pm, \mp} |\langle \phi_i^{\pm, \mp} | \{J_x, J_y, J_z\} | \phi_0^\pm \rangle|^2. \quad (4)$$

The crystal-field parameters B_n^m for NaYbO₂ in Eq. (1) can first be estimated within a simple point-charge model and then established with fits to energy cuts through inelastic neutron-scattering data. While point-charge models are rarely accurate, they often provide a physically grounded starting point to determine B_n^m parameters when fitting limited scattering data. The point-charge model for NaYbO₂ was calculated with the following formula as implemented in the crystal-field interface of MANTIDPLOT [65]:

$$B_n^m = \frac{4\pi}{2n+1} \frac{|e|^2}{4\pi\epsilon_0} \sum_i \frac{q_i}{r_i^{n+1}} a_0^n \langle r^n \rangle Z_n^m(\theta_i, \phi_i). \quad (5)$$

The point-charge model takes into account the polar location (r_i, θ_i, ϕ_i) of the i th charge q_i relative to the central Yb ion where $\langle r^n \rangle$ is the n th-order expectation value of the Yb

TABLE I. point-charge (PC) models and CEF fits for NaYbO₂ compared to observed eigenenergies and intensities from $E_i = 150$ meV INS data and anisotropic g factors [54] with corresponding CEF wavefunctions. PC (3.0 Å) incorporates only O²⁻ ions in local YbO₆ D_{3D} distorted octahedra into calculations (one coordinate shell), while PC (3.5 Å) additionally includes nearest-neighbor Yb³⁺ ions and Na⁺ ions (two coordinate shells) as shown in Fig. 1. Fit 1 reproduces observables with a lower χ^2 value in comparison to Fit 2. However, Fit 2 resembles the signs of PC (3.5 Å) except B_6^0 which is relatively small.

	E_1	E_2	E_3	$\frac{I_2}{I_1}$	$\frac{I_3}{I_1}$	g_c	g_{ab}	χ^2	B_2^0	B_4^0	B_6^0	B_4^3	B_6^3	B_6^6
PC (3.0 Å)	70.5	146.4	191.5	0.037	0.033	7.86	0.36	342.0	-5.0675	0.016956	0.00015465	-0.64149	-0.00034913	0.0014353
PC (3.5 Å)	19.2	35.8	87.5	0.588	0.061	0.83	3.44	16.5	1.6302	0.020578	0.00017436	-0.66203	-0.00022040	0.0017501
Fit 1	34.0	58.4	82.5	0.579	0.880	1.70	3.38	0.005	-0.79877	0.00085658	0.0028000	0.51143	0.011036	0.015580
Fit 2	33.8	58.3	82.5	0.574	0.845	1.68	3.48	0.012	0.28257	0.0058508	-0.00055392	-0.76448	-0.010493	0.025079
Observed	33.9	58.2	82.6	0.548	0.866	1.72	3.30							

Fit 1	
$ \omega_{0,\pm}\rangle =$	$-0.029 \mp 1/2\rangle \mp 0.496 \pm 1/2\rangle - 0.578 \mp 5/2\rangle \pm 0.034 \pm 5/2\rangle \mp 0.038 \mp 7/2\rangle + 0.646 \pm 7/2\rangle$
$ \omega_{1,\pm}\rangle =$	$-0.001 \mp 1/2\rangle \mp 0.473 \pm 1/2\rangle + 0.805 \mp 5/2\rangle \mp 0.002 \pm 5/2\rangle \mp 0.001 \mp 7/2\rangle + 0.358 \pm 7/2\rangle$
$ \omega_{2,\pm}\rangle =$	$\pm 0.025 \mp 1/2\rangle + 0.727 \pm 1/2\rangle \pm 0.128 \mp 5/2\rangle - 0.004 \pm 5/2\rangle - 0.023 \mp 7/2\rangle \pm 0.673 \pm 7/2\rangle$
$ \omega_{3,\pm}\rangle =$	$\pm 0.614 \mp 3/2\rangle + 0.789 \pm 3/2\rangle$

Fit 2	
$ \omega_{0,\pm}\rangle =$	$0.075 \mp 1/2\rangle \pm 0.582 \pm 1/2\rangle - 0.528 \mp 5/2\rangle \pm 0.068 \pm 5/2\rangle \mp 0.078 \mp 7/2\rangle + 0.604 \pm 7/2\rangle$
$ \omega_{1,\pm}\rangle =$	$1 \pm 3/2\rangle$
$ \omega_{2,\pm}\rangle =$	$\mp 0.574 \mp 1/2\rangle - 0.034 \pm 1/2\rangle \mp 0.047 \mp 5/2\rangle + 0.803 \pm 5/2\rangle + 0.149 \mp 7/2\rangle \mp 0.009 \pm 7/2\rangle$
$ \omega_{3,\pm}\rangle =$	$-0.004 \mp 1/2\rangle \mp 0.570 \pm 1/2\rangle + 0.263 \mp 5/2\rangle \mp 0.002 \pm 5/2\rangle \mp 0.005 \mp 7/2\rangle + 0.779 \pm 7/2\rangle$

radial wave function, Z_n^m is a spherical tesseral harmonic, ϵ_0 is the permittivity of free space, $|e|$ is the elemental charge, and a_0 is the Bohr radius. Point-charge calculations including one coordination shell (≤ 3.0 Å; O²⁻ ions) and two coordination shells (≤ 3.5 Å; O²⁻, Yb³⁺, Na⁺ ions) are shown in Table I.

Models were evaluated utilizing a combination of the crystal-field interface of MANTIDPLOT [65], SPECTRE [66], and numerical error minimization that combined scattering data with magnetic measurements. A general minimization procedure [41,67] follows this loop.

(1) Initialize the Hamiltonian with a guess of CEF parameters, either from related compounds (e.g., YbMgGaO₄ [41]) or a point-charge model.

(2) Diagonalize the CEF Hamiltonian (1), and obtain energy eigenvalues, ground-state wave functions, g factors, and relative intensity ratios.

(3) Calculate $\chi_{\text{tot}}^2 = \chi_{\text{energies}}^2 + \chi_g^2 + \chi_{\text{intensities}}^2$, where $\chi^2 = \sum \frac{(\text{obs}-\text{calc})^2}{\text{calc}}$ and χ_g^2 reflects the deviations of calculated g factors, $\chi_{\text{intensities}}^2$ reflects the deviation of calculated intensities of transitions, and χ_{energies}^2 reflects deviations of calculated energy levels.

(4) Modify CEF parameter(s) and reiterate. Accept the new parameters if $\chi_{\text{tot, new}}^2 < \chi_{\text{tot, old}}^2$.

This sequence was then iterated to obtain a global minimum that best represents the observed data.

D. Spin-wave analysis

We calculate the dynamic spin structure factor $S(\mathbf{q}, \omega)$ as a function of energy and momentum. The detailed derivation has been given in [54], and here we only outline the procedures. Starting from the spin model (6) ($D = 0$), we numerically minimize the energy to obtain the classical ground state, and then use the standard Holstein-Primakoff method

to construct a spin-wave Hamiltonian, the diagonalization of which gives the magnon modes. A spin-spin correlation function is then readily obtained, the momentum Fourier transform of which gives the desired quantity $\mathcal{S}(\mathbf{q}, \omega)$. Note that in order to simulate the powder sample results we take the average over all momentum directions and then all magnetic field orientations, and we denote the final result after the two-step average as $\overline{\mathcal{S}}(Q, \omega)$. Note the two averages are done completely *independently*. Admittedly, such a simulated spin structure factor does not fully mimic the experimental situation, since in reality the measurement just amounts to a one-time average over the grain orientations of the powder sample, and during the averaging process the rotations of the momentum and magnetic field are *locked*. However, our choice of averaging is justified by the robust spectral features observed in a large region with easy-plane near-Heisenberg exchange.

III. EXPERIMENTAL RESULTS

A. High-energy crystalline electric-field excitations

Inelastic neutron-scattering (INS) data collected at $T = 5$ K with an $E_i = 150$ meV are shown in Fig. 2(a), revealing three CEF excitations out of the ground-state doublet. The lowest-lying excitation is centered at $E_1 = 33.9$ meV, which is consistent with a well-separated ground-state Kramers doublet, and the second and third excited states are observed centered at $E_2 = 58.2$ and $E_3 = 82.6$ meV, respectively. CEF excitation energies, integrated intensity ratios, and g -tensor components [54] are displayed with point-charge models and CEF fits to integrated $S(\mathbf{Q}, \hbar\omega)$ cuts of the data in Table I.

Models converged toward two minima labeled as “Fit 1” and “Fit 2” shown in Table I. Fit 1 is unconstrained and has the lowest global error, however we note that it deviates strongly

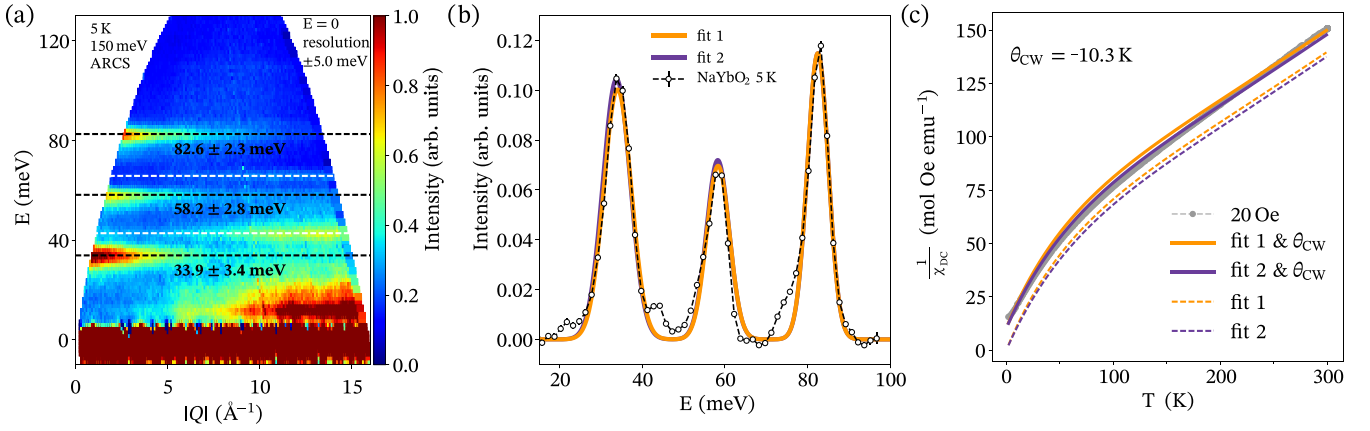


FIG. 2. (a) INS spectrum $S(Q, \hbar\omega)$ at 5 K obtained on ARCS at the Spallation Neutron Source with $E_i = 150$ meV. The three dashed black lines feature the three CEF excitations while the dashed white lines correspond to phonons seen in integrated cuts in panel (b). Uncertainties specified next to energy values are the calculated instrument energy resolutions at those energies. (b) Experimental fits to the $|Q| = [3.0, 3.5]$ \AA^{-1} integrated cut at 5 K of the INS spectrum. Fit 1 has the lowest χ^2 value to INS data (Table I), while fit 2 closely resembles a point-charge model incorporating two coordination shells (I). (c) Inverse magnetic susceptibility of NaYbO_2 at 20 Oe overlaid with calculated inverse magnetic susceptibilities from two comparable CEF models. The mean-field exchange interaction is introduced (solid lines) to account for deviations due to strong antiferromagnetic exchange in NaYbO_2 [54]. Calculated susceptibilities that do not include the antiferromagnetic interaction (dashed lines) do not accurately reproduce the data.

from point-charge models. If the signs of the crystal-field parameters (excluding B_0^0) are enforced to agree with a two-shell point-charge model that includes O^{2-} , Yb^{3+} , and Na^+ ions (PC 2 in Table I), then fit 2 provides the best solution. It should be noted that a point-charge model incorporating only one coordination shell of O^{2-} ions (PC 1 in Table I) could not be optimized to represent any of the observed data. Therefore, the Coulomb environment surrounding Yb ions in NaYbO_2 is heavily influenced by ions beyond the first coordination shell, consistent with recent theoretical analysis [68].

Figure 2(b) shows a comparison of the magnetic susceptibility data [54] with the two models obtained from INS analysis calculated with the crystal-field interface in MANTIDPLOT [65]. The susceptibilities calculated from the INS fits do not fully capture the data, and instead a modified effective susceptibility χ_{eff} that includes antiferromagnetic exchange must be introduced: $\chi_{\text{eff}} = \frac{\chi_{\text{calc}}(T)}{1 - \theta_{\text{CW}} \chi_{\text{calc}}(T)}$. Here, the previously determined antiferromagnetic exchange interaction $\theta_{\text{CW}} = -10.3$ K [54] was used in Fig. 2(b).

Additionally, the moment size of each model for the ground-state doublet was determined within MANTIDPLOT [65] via adding a Zeeman interaction to the CEF Hamiltonian to compare with the ordered moment in the up-up-down phase previously determined for NaYbO_2 [54]. At $B = 5$ T, the expected powder-averaged moment of fit 1 is $1.43 \mu_B$ and that of fit 2 is $1.49 \mu_B$. These values are 5.15 and 9.56% larger than the observed moment in our previous study of $1.36(1) \mu_B$ [54], potentially reflective of a fluctuation-reduced moment.

With a lower $E_i = 60$ meV, the INS spectrum at $T = 5$ K only contains a single excitation out of the lowest-lying Kramers doublet as shown in Fig. 3. In this higher-energy resolution setup, it becomes clear that the first excited doublet consists of two asymmetrically split, resolution-limited peaks with centers at 35.5 ± 1.3 and 33.4 ± 1.4 meV. This splitting of approximately $\Delta E = 2.1$ meV is too narrow to observe

in the higher $E_i = 150$ meV data of Fig. 2. For comparison, instrumental resolutions at both energy transfers are tabulated in Fig. 1(c) as errors in observed CEF excitation peak centers. Splitting of the lowest-lying doublet is naively not allowed in the CEF Hamiltonian from Eq. (1) by Kramers theorem and the D_{3D} Yb ion point-group symmetry. While such a splitting can indicate two different Yb local environments in the lattice, earlier diffraction studies do not resolve this or other modes of average chemical disorder [54]. Instead, the CEF Hamiltonian neglects any interactions beyond the single-ion level, such as exchange-induced dispersion [69], which is the likely origin of the splitting and a further reflection of the sizable Yb-exchange interactions in this material. We note here though that more complicated forms of disorder in the local structure generating this CEF splitting cannot be completely excluded by the present data.

B. Low-energy magnetic excitations

In order to investigate the correlated spin dynamics of the Yb moments, low-energy inelastic neutron-scattering measurements were performed below 100 mK. Figure 4 and Figs. S1 and S2 of Supplemental Material [70] show the field-dependent evolution of the INS spectrum of NaYbO_2 powder across a series of fields spanning from 0 to 10 T. $H = 0, 5$, and 10 T data sets were counted approximately eight times longer relative to other fields in Fig. 4, and the temperature stabilized between $T = 67$ and 100 mK across this field range.

At zero field, NaYbO_2 contains a continuum of excitations from the quantum disordered ground state that evolve into the up-up-down ordered phase as previously reported [54]. The diffuse continuum is centered about the two-dimensional magnetic zone center $\mathbf{Q} = (1/3, 1/3, 0)$ with a bandwidth of approximately 1 meV. With increasing field at base temperature, the spectral weight condenses and splits, with part of it

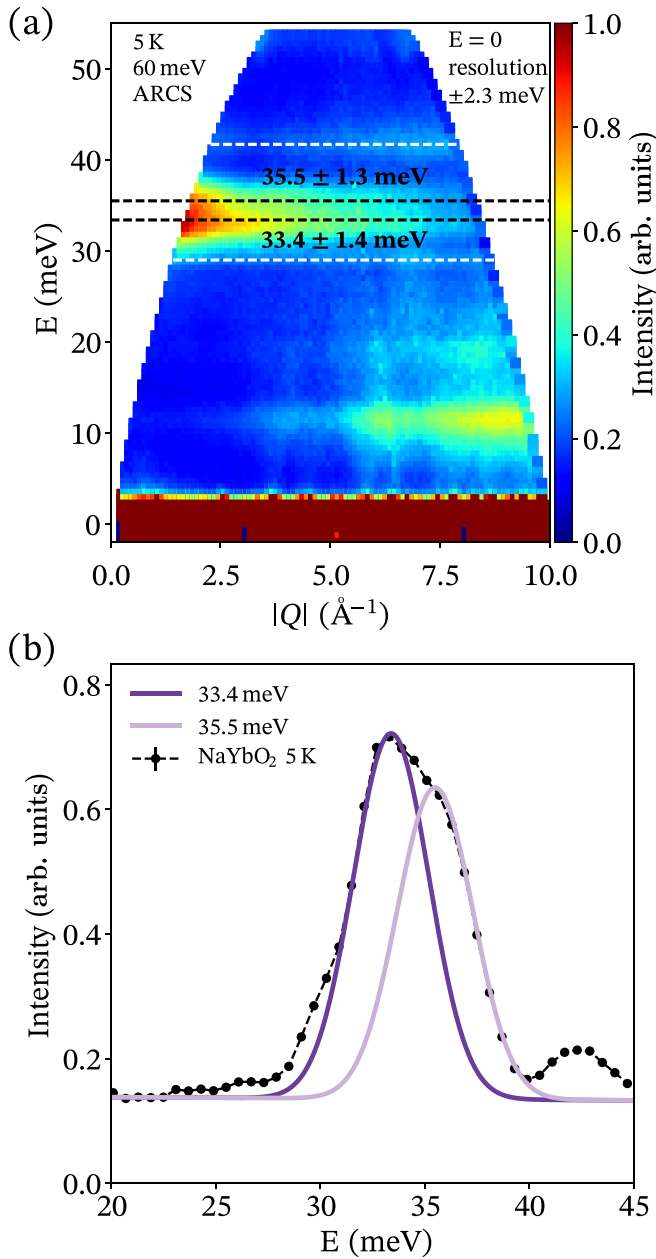


FIG. 3. (a) INS spectrum $S(Q, \hbar\omega)$ at 5 K obtained on ARCS at the Spallation Neutron Source with $E_i = 60$ meV. The two dashed black lines indicate the split peak observable at $E_i = 60$ meV, and the dashed white lines correspond to nearby phonons. Uncertainties specified next to energy values are the calculated instrument energy resolutions at those energies. (b) $|Q|$ integrated cut of the 5-K INS spectrum from $[2.5, 3] \text{ \AA}^{-1}$ illustrating that the first CEF excitation in NaYbO_2 is broadened by exchange-induced CEF dispersions. Fits to two resolution-limited Gaussian peaks separated by 2.1 meV accurately capture the splitting. The instrumental resolution is denoted by error bars beneath each peak.

coalescing into the elastic line and part of it pushed upward within a nearly flat, powder-averaged band near 1 meV in the ordered state (Fig. 4). Upon exiting the ordered state at 10 T, the remaining resolvable scattering in this energy window primarily resides above the two-dimensional magnetic zone

center $\mathbf{Q} = (1/3, 1/3, 0)$ ($|\mathbf{Q}| = 1.25 \text{ \AA}^{-1}$) and the $(0,0,3)$ Bragg peak ($|\mathbf{Q}| = 1.15 \text{ \AA}^{-1}$).

Figure 5 further parametrizes the spectral shift under field via momentum-averaged energy cuts. In Fig. 5(a) the low-energy spectral weight endemic to the zero-field quantum disordered ground state can be seen to diminish and pushes upward in energy with increasing field. Data integrated about the two-dimensional magnetic zone center $\mathbf{Q} = (1/3, 1/3, 0)$ show a pile-up of spectral weight near $E_{\text{peak}} = 0.25$ meV in the quantum disordered phase which continuously shifts upward upon approaching the ordered phase. Prior heat-capacity data [54] demonstrate that gapless excitations necessarily persist below this peak in the fluctuation spectrum, and it is reminiscent of deconfined spinons coexisting with fluctuations associated with short-range antiferromagnetic correlations simulated in variational Monte Carlo studies of triangular lattice models [71].

Looking at higher energies, Fig. 5(b) illustrates the upward shift of the flat band of powder-averaged modes associated with up-up-down order. Increasing the field pushes the high-frequency mode upward consistent with linear spin-wave calculations discussed later in this paper and with prior nonlinear spin-wave treatment of the up-up-down state [72]. Upon approaching the upper-field phase boundary for the up-up-down state, this band broadens and diminishes, while a second lower band appears near $E = 0.5$ meV and shifts downward in energy with increasing field. This suggests a softening of at least one branch of modes within the up-up-down state toward the upper-field boundary and disappearance of magnetic order. It may also presage the existence of an upper-field phase boundary into another ordered state.

A third, anomalous, feature appears in energy cuts through the $\mathbf{Q} = (1/3, 1/3, 0)$ position in Fig. 5(a). Upon entering the up-up-down phase, spectral weight appears at an energy near $E = 1.5$ meV which is $\approx 3J$ and far above the expected single-magnon cutoff. This peak, which we label E^* , appears in the fully formed up-up-down state [54] and suggests substantial spectral weight within the multimagnon scattering channel or an unconventional spin-wave mode pulled out of the continuum [73]. If the origin is two-magnon scattering, substantial weight present in the longitudinal channel of spin fluctuations indicates strong magnon-magnon interactions in this material and would be consistent with the reduction in the ordered moment due to strong quantum fluctuations.

C. Field-dependent magnetic order

Upon analyzing the elastic line ($E = 0$ meV) in Fig. 6, the onset of static magnetic order in NaYbO_2 under applied field can be observed. At 5 T, peaks appear at momentum transfers corresponding to the $\mathbf{Q} = (1/3, 1/3, z)$ positions as shown in Fig. 6(a). The onset and subsequent exit of three-sublattice order upon cycling the magnetic field upward from 0 to 10 T can be monitored via the $\mathbf{Q} = (1/3, 1/3, 0)$ reflection shown in Fig. 6. This is the strongest magnetic reflection that does not coincide with a structural Bragg peak, and it is present in both the collinear up-up-down state as well as in other noncollinear states such as the canted V-state and Y-state order detailed in Sec. IV of this paper. The intensity of this peak is shown in Fig. 6(b) for a field ramp up at $H = 0, 5,$

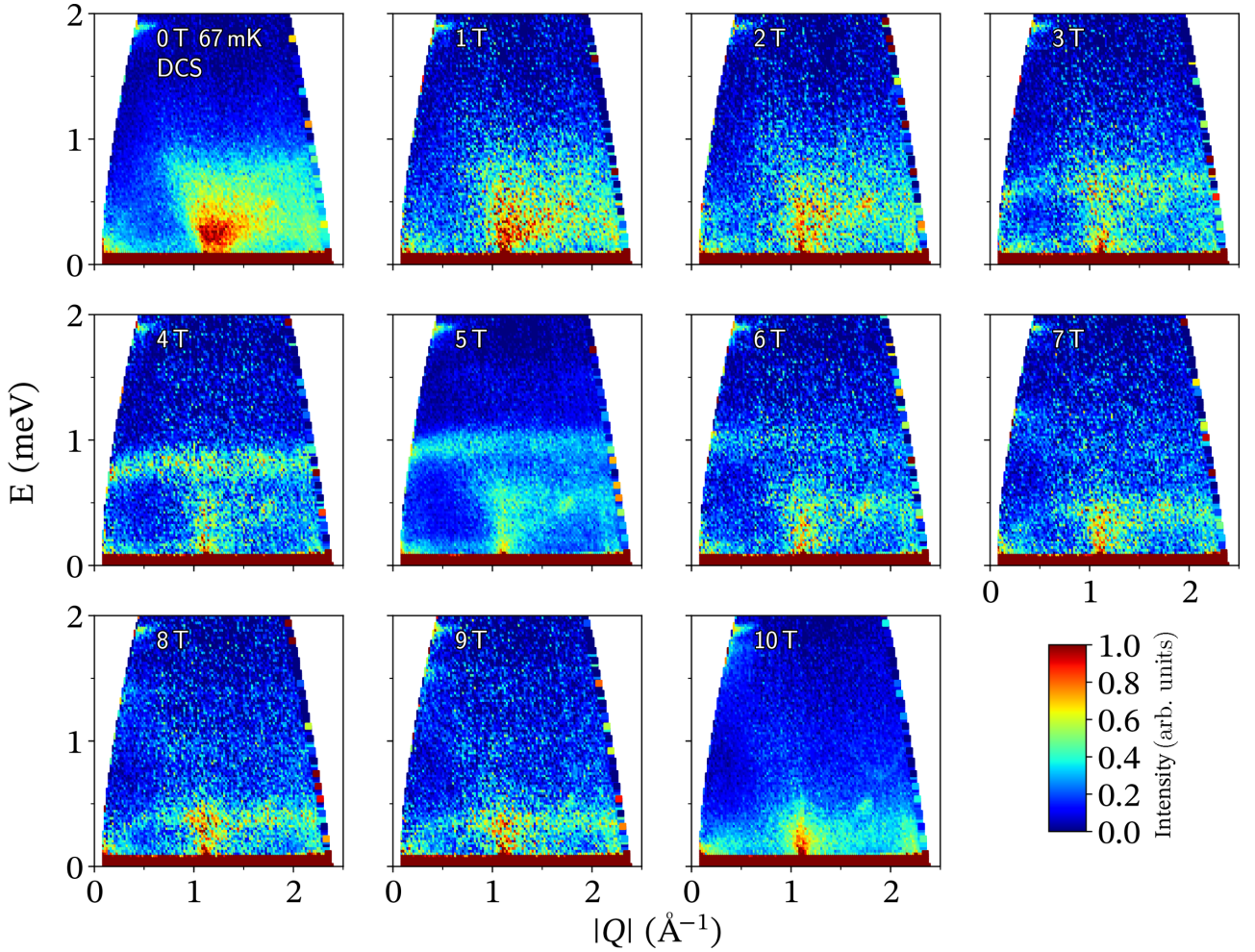


FIG. 4. Low-energy INS spectrum $S(Q, \hbar\omega)$ of NaYbO_2 powder at varying fields collected on DCS. With increasing field, NaYbO_2 evolves from a gapless quantum disordered ground state (0–2 T) into an up-up-down equal moment magnetic structure (3–8 T) and a field-polarized state at high field (9–10 T). Data were collected with longer scans at 0, 5, and 10 T to increase resolution. Detector spurious occur at $[0.5 \text{ \AA}^{-1}, 1.8 \text{ meV}]$ and $[1.75 \text{ \AA}^{-1}, 0.4 \text{ meV}]$. Data were collected between 67 and 100 mK.

and 10 T and for a field ramp down from 9 to 2 T. Data points at 0 and 10 T are placed for reference, as no integrable intensity is present at those fields. As previously determined with ac susceptibility [54], the powder-averaged boundary of field-induced magnetic order resides between 2–3 and 8–9 T, which coincides with the onset and disappearance of the $\mathbf{Q} = (1/3, 1/3, 0)$ peak.

Surprisingly, after cycling the NaYbO_2 powder to 10 T and then returning down to 5 T, the magnetic order stabilized changes. Specifically, the $\mathbf{Q} = (1/3, 1/3, 2)$ peak, previously absent on cycling the field upward and the suppression of which is indicative of collinear up-up-down order, appears upon cycling the field downward. This new peak coincides with the onset of the $\mathbf{Q} = (1/3, 1/3, 0)$ peak, and the field evolution of the $\mathbf{Q} = (1/3, 1/3, 2)$ peak is displayed in Fig. 6(c). This hysteresis in the onset of magnetic order upon traversing the upper-field phase boundary from above suggests a first-order phase line and the appearance of a noncollinear ordered state. Recent calculations have predicted such a phase boundary into a coplanar V state in triangular lattice systems with strong interplanar exchange coupling

[74]; however, identifying the precise spin structure trapped across this first-order phase line requires future single-crystal measurements.

IV. THEORETICAL ANALYSIS

A. Classical 2D XXZ model

In this section we further the study of the classical phase diagram of the 2D XXZ model on the triangular lattice in the presence of a field along an arbitrary direction. The Hamiltonian reads

$$H = \sum_{(i,j)} J_z S_i^z S_j^z + J_{xy} (S_i^x S_j^x + S_i^y S_j^y) + D \sum_i (S_i^z)^2 - \sum_i \mu_B g_{\mu\nu} B^\mu S_i^\nu, \quad (6)$$

where $\mu, \nu = x, y, z$, $g_{\mu\nu} = \text{diag}(g_{xy}, g_{xy}, g_z)$. We have shown in [54] that the four-term Hamiltonian representing the 2D XXZ model reduces to this one, assuming three-sublattice order. The main conclusions from our previous study [54]

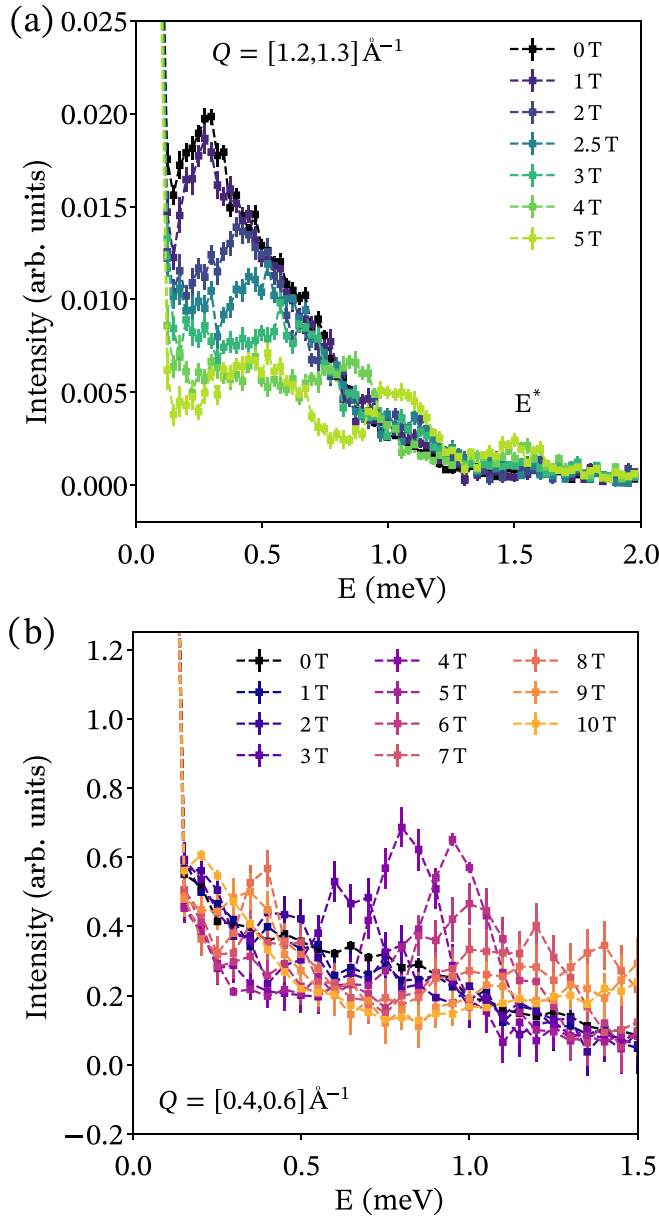


FIG. 5. (a) Low-energy INS of NaYbO₂ from CNCS at 5 T plotted on a logarithmic scale showing a weak third magnetic peak (E^*) centered at 1.5 meV above the flat, powder-averaged bands from the up-up-down phase. The third magnetic mode arises from a multimagnon process convolving the two lower-energy bands of the up-up-down phase. At 5 T, this multimagnon band is readily visible as it is well separated from the powder-averaged up-up-down structure. (b) Low $|Q|$ -integrated energy cut of INS data of NaYbO₂ from DCS data (4) showing the evolution of the flat up-up-down mode as a function of field.

of this Hamiltonian are that (1) the ground state is a three-sublattice 120° structure that (2) evolves into a canted phase with an external field, which becomes a canted up-up-down structure depending on the field strength and direction, and (3) a good fit to the inelastic neutron-scattering powder-averaged spectrum of NaYbO₂ is produced at $J_{xy} = 0.51$ meV and $J_z = 0.45$ meV.

We now use $d = a, b, c$ to label the three sublattices, and define $S_d^\mu = S n_d^\mu$, where \mathbf{n}_d is a unit vector. We further define $\Sigma^\mu = \sum_d n_d^\mu$; then the classical ground state is obtained by minimizing the following quantity:

$$E = \frac{H}{3NS^2J_{xy}/2} = A(\Sigma^z - h_z)^2 + (\Sigma^x - h_x)^2 + (\Sigma^y - h_y)^2 - \delta \sum_d (s_d^z)^2 - C, \quad (7)$$

where N is the number of sites in the 2D lattice, and we have defined

$$A = \frac{J_z}{J_{xy}}, \quad (h_x, h_y, h_z) = \frac{\mu_B}{3S} \left(\frac{g_{xy}B^x}{J_{xy}}, \frac{g_{xy}B^y}{J_{xy}}, \frac{g_zB^z}{J_z} \right),$$

$$\delta = A - 1 - \frac{2D}{3J_{xy}}, \quad C = \frac{\frac{H_z^2 J_{xy}}{3J_z^2} + \frac{H_y^2}{3J_{xy}} - 9J_{xy}S^2}{3S^2J_{xy}}. \quad (8)$$

We then write $\mathbf{n}_d = (\sin \theta_d \cos \phi_d, \sin \theta_d \sin \phi_d, \cos \theta_d)$ and take the derivatives with respect to angular variables:

$$\frac{\partial E}{\partial \theta_d} = 0 \Rightarrow -2A(\Sigma^z - h_z)s_d^{xy} + 2(\Sigma^x - h_x)s_d^z \frac{s_d^x}{s_d^{xy}} \quad (9a)$$

$$+ 2(\Sigma^y - h_y)s_d^z \frac{s_d^y}{s_d^{xy}} + 2\delta s_d^z s_d^{xy} = 0, \quad (9b)$$

$$\frac{\partial E}{\partial \phi_d} = 0 \Rightarrow -2(\Sigma^x - h_x)s_d^y + 2(\Sigma^y - h_y)s_d^x = 0, \quad (9c)$$

where $s_d^{xy} = (s_d^x)^2 + (s_d^y)^2$ (we will use similar notation for other quantities). We then have the following two cases.

1. Case 1

If $\Sigma^x - h_x$ and $\Sigma^y - h_y$ do not vanish at the same time, suppose $\Sigma^y - h_y \neq 0$; then we have $\frac{\Sigma^x - h_x}{\Sigma^y - h_y} = \frac{s_d^x}{s_d^y}$; the order is coplanar in the plane containing the z axis. Therefore we are actually minimizing

$$E_{\text{coplanar}} = A(\Sigma^z - h_z)^2 + (\Sigma^{xy} - h_{xy})^2 - \delta \sum_d (s_d^z)^2. \quad (10)$$

This will be treated in detail below.

2. Case 2

Otherwise, we have

$$\Sigma^x - h_x = \Sigma^y - h_y = 0. \quad (11)$$

Plugging this into Eq. (9b), we see that

$$s_d^{xy} [\delta s_d^z - A(\Sigma^z - h_z)] = 0 \quad (12)$$

has four cases, depending on how many $s_d^{xy} = 0$; note that if two or all three $s_d^{xy} = 0$ then the situation is included in the first case. Therefore we only need analyze two possibilities.

The first is if $s_d^{xy} \neq 0$ for all $d = a, b, c$ then we must have

$$s_a^z = s_b^z = s_c^z = \frac{Ah_z}{\delta - 3A}. \quad (13)$$

In other words, the spins have equal z component. We call this the ‘‘canted-I’’ phase. This solution should be considered only

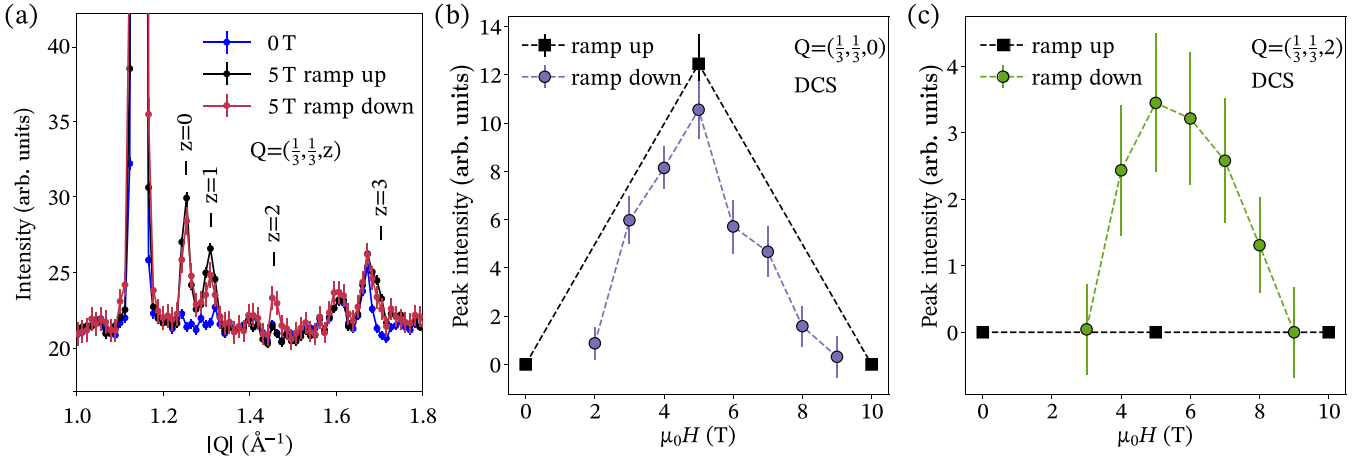


FIG. 6. (a) Neutron powder-diffraction data collected from an elastic line cut on the DCS instrument at the NIST Center for Neutron Research with 5-\AA incident neutrons between $E = [-1, 1]$ meV. In zero field, no new magnetic reflections arise. Data at 0 T were collected at 67 mK and 5-T data were collected at 74 mK. (b, c) Integrated intensity of the $Q = (1/3, 1/3, 0)$ and $(1/3, 1/3, 2)$ peaks, respectively, upon sweeping the field from $0 \rightarrow 10$ T and $10 \rightarrow 0$ T between 67 mK (0 T) and 92 mK (10 T). Data were analyzed via Gaussian fits to elastic line DCS data. At 0 and 10 T, there was no observable intensity at the $Q = (1/3, 1/3, 0)$ position, indicating NaYbO_2 is in its quantum disordered ground state and field-polarized state, respectively. No quantifiable intensity is ascribable to the $Q = (1/3, 1/3, 2)$ peak on field ramping from $0 \rightarrow 10$ T. However, upon ramping downward, $10 \rightarrow 0$ T, the $Q = (1/3, 1/3, 2)$ peak appears between 9 and 3 T.

when $s^z = |\frac{A h_z}{\delta - 3A}| \leq 1$ and $3\sqrt{1 - (s^z)^2} \leq h_{xy}$, i.e.,

$$\frac{h_{xy}^2}{9} + \frac{h_z^2}{(3 - \delta/A)^2} \leq 1. \quad (14)$$

The ground-state manifold is a degenerate one-dimensional (1D) parameter space, resulting from the different ways the xy in-plane vectors satisfy Eq. (11). Note that in this case the three equations for θ_d are all independent, but the three equations for ϕ_d are reduced to just two equations. Therefore we should get a 1D degenerate classical ground-state manifold.

The second possibility is to suppose $s_a^{xy} = 0$ and $s_b^{xy} = s_c^{xy} \equiv s^{xy} \neq 0$; then we must have $s_b^z = s_c^z$. We call this the “canted-II” phase. In this case there are already four equations; therefore, the spins are uniquely determined, leaving no classical ground-state degeneracy. This solution should be considered only when $s^{xy} = \sqrt{1 - (s^z)^2} \geq h_{xy}/2$, i.e.,

$$\frac{h_{xy}^2}{4} + \frac{(s_a^z - h_z)^2}{(2 - \delta/A)^2} \leq 1, \quad s_a^z = \pm 1. \quad (15)$$

In summary, the classical ground state of the Hamiltonian (6) can only be one of the following types: coplanar (in which the order plane must contain the z axis), collinear, canted-I (in which the three spins have the same z component), or canted-II (in which one spin lies along z and the other two have the same z component). For generic field directions, only the canted-I states can form a 1D degenerate classical ground-state manifold.

B. Classical phase diagram

In the following we will set the onsite ion term $D = 0$, which means $\delta = A - 1$. We now present a concrete phase

diagram for the Hamiltonian in the (A, h_{xy}, h_z) phase space. For an illustration of the phase diagram, see Fig. 7.

1. Easy-plane anisotropy

In the easy-plane anisotropy region ($0 < A < 1$), the phase diagram has been analytically obtained [54]:

$$\begin{cases} \frac{h_{xy}^2}{9} + \frac{h_z^2}{(1/A+2)^2} \geq 1 : & \text{paramagnetic phase;} \\ \frac{h_{xy}^2}{9} + \frac{h_z^2}{(1/A+2)^2} < 1 : & \text{canted-I phase.} \end{cases} \quad (16)$$

The phase boundary is the same as Eq. (14) if we take the equality. The “paramagnetic” phase has a unique classical ground state while in the canted-I phase the classical ground states are accidentally degenerate and form a one-dimensional manifold, subject to the constraints (11) and (13).

2. Easy-axis anisotropy

In the easy-axis anisotropy region ($A > 1$), three phases exist: the paramagnetic phase, the “Y” phase, and the “V” phase. We define the V phase to be such that two of the spins have identical orientation which is different from the third one, while we define the Y phase to be such that the orientation of each is different from the other two. In [54] we were able to find the boundary that separates the paramagnetic phase from the V and the Y phases, but were unable to find the phase boundary between the latter two. Here we provide the complete phase diagram:

$$\begin{cases} \frac{h_{xy}^2}{(A+2)^2} + \frac{h_z^2}{(1/A+2)^2} \geq 1 : & \text{paramagnetic phase;} \\ \frac{h_{xy}^2}{(A+2)^2} + \frac{h_z^2}{(1/A+2)^2} < 1 : & \text{V phase;} \\ \text{and } h_z \geq h_{z,0}(A, h_{xy}) & \\ h_z \leq h_{z,0}(A, h_{xy}) : & \text{Y phase,} \end{cases} \quad (17)$$

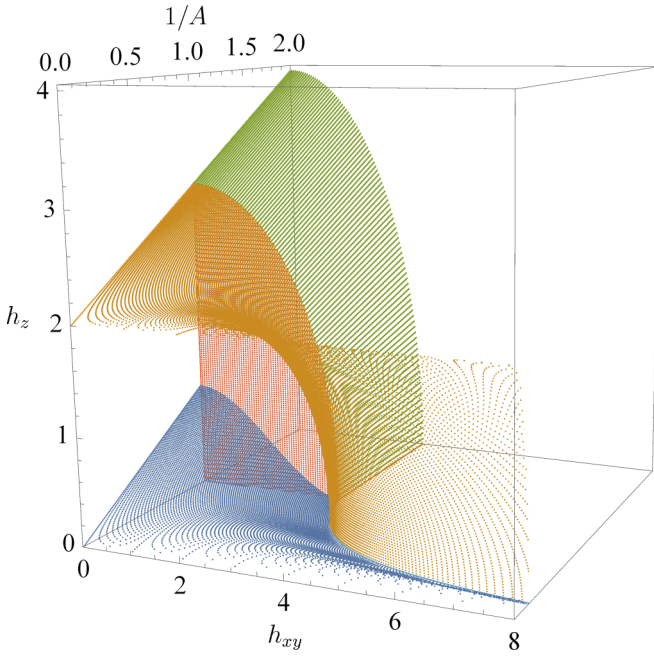


FIG. 7. Classical phase diagram of the 2D XXZ model on a triangular lattice in the presence of magnetic field. The 3D phase space is parametrized by (h_{xy}, A^{-1}, h_z) , where $h_{xy} = \sqrt{h_x^2 + h_y^2}$. Only the first octant ($h_{xy} \geq 0, A^{-1} \geq 0, h_z \geq 0$) is considered. The blue surface separates the Y and the V phases; the red plane separates the phases between the $A < 1$ and the $A > 1$ regions; the green surface separates the canted-I and the paramagnetic phases in the region $A < 1$, and the orange surface separates the V and the paramagnetic phases in the region $A > 1$.

where we have defined critical $h_{z,0}(A, h_{xy})$, which is a function of A and h_{xy} . $h_{z,0}$ is determined from the following group of equations, taking the smallest positive nonzero solution for $h_{z,0}$:

$$\begin{aligned} A(a + c - h_z)\sqrt{1 - a^2} &= a(\sqrt{1 - a^2} + \sqrt{1 - c^2} - h_{xy}), \\ A(2a - h_z)\sqrt{1 - c^2} &= c(2\sqrt{1 - a^2} - h_{xy}), \\ c &= h_z - a^3(A^{-1} - 1) - 2a. \end{aligned} \quad (18)$$

The corresponding solution for the other variables $a = n_a^z = n_b^z$ and $c = n_c^z$ gives the z component of the three spins in the V phase. The first two equations simply come from the saddle-point equation (9b); the last equation originates from the fact that at the vicinity of the phase boundary between V and Y the energy (10) (note now $\delta = A - 1$) takes the form $E_{\text{coplanar}} \sim \text{const} + O(a - b)^3$, i.e., when expanding E_{coplanar} in powers of $a - b$ both the first- and second-order terms must vanish (in fact the third-order term vanishes too). The analytical solution of Eqs. (18) to h_z is hard; however, when A is small enough ($A < 2$ for a numerical estimation), the solution for h_z can be well approximated by the empirical form

$$h_z = \frac{1}{A} \left(1 - \frac{h_x}{2+A}\right)^2 \left[b + (1-b) \left(1 - \frac{h_x}{2+A}\right) \right]^2 \quad (19)$$

with appropriate choice of b as a fitting parameter. Note in the limit $h_{xy} = 0$ (perpendicular field) we recover the result

$h_{z,0} = 1/A$ for the boundary between the Y and the V phases, and $h_{z,1} \equiv 1/A + 2$ for the boundary between the V phase and the fully polarized phase [75]. Note also that a special type of the V state, the up-up-down state, should be distinguished as another distinct phase in the $h_{xy} = 0$ limit, but such a phase loses its meaning as soon as an in-plane field component is turned on.

Applying these results to NaYbO_2 , which carries easy-plane exchange couplings $J_z = 0.45$ meV and $J_{xy} = 0.51$ meV, we are left only with two phases: the canted-I phase and the paramagnetic phase. The critical field for the onset of the paramagnetic phase is

$$B_{z,c} = 21.15 \text{ T}, \quad B_{xy,c} = 12.03 \text{ T}, \quad (20)$$

and when the field is oriented in other directions the corresponding critical B_c interpolates between these two values.

We note here that the canted-I phase does not exactly match the experimentally reported up-up-down state. A slightly canted up-up-down state can, however, form within the manifold of allowed canted-I states. This may be beyond the detection of the current powder measurements, or, alternatively, we envision that quantum fluctuations or other exchange interactions may lead to a slightly different ground state from those predicted in the purely 2D classical XXZ phase diagram. Despite this difference, the dynamics calculated from the classical 2D model are likely to be relatively insensitive to small differences in the ordered phase such as a small degree of noncollinear canting predicted in the present model.

C. Spin-wave analysis

The two-step averaged dynamic spin structure factor $\overline{\overline{S}}(\mathbf{Q}, \omega)$ for various field strengths is plotted in Fig. 8. As we expect that the ground state of NaYbO_2 is strongly renormalized by quantum fluctuations, this model only captures features in the field-induced ordered state of NaYbO_2 where quantum fluctuations in the material are suppressed. Three main features can be observed immediately.

1. Region I

Zero energy intensity at the two-dimensional magnetic zone center $\mathbf{Q} = (1/3, 1/3, 0)$ ($|\mathbf{Q}| = 1.25 \text{ \AA}^{-1}$) can be observed for a large range of field values, indicating the existence of the gapless Goldstone mode at the Γ point. The zero energy intensity is the highest at zero field with a sharp linear dispersion, and, as the field starts to increase, such zero energy intensity decreases, while the intensity at low but finite energy begins to develop. The zero energy intensity becomes extremely weak but still observable as the field goes beyond 13 T, and finally vanishes entirely at high-field values 22 T. Such behavior of the gapless intensities can be understood from the classical ground state: the ground state belongs to the canted-I phase, which forms a 1D degenerate ground-state manifold and possesses one Goldstone mode for generic field directions and strength. As the field increases, the configuration with the in-plane field first reaches a critical field at 12 T, and the structure factor of such configuration becomes gapped due to the vanishing of Goldstone modes. As the field further increases, more and more configurations reach

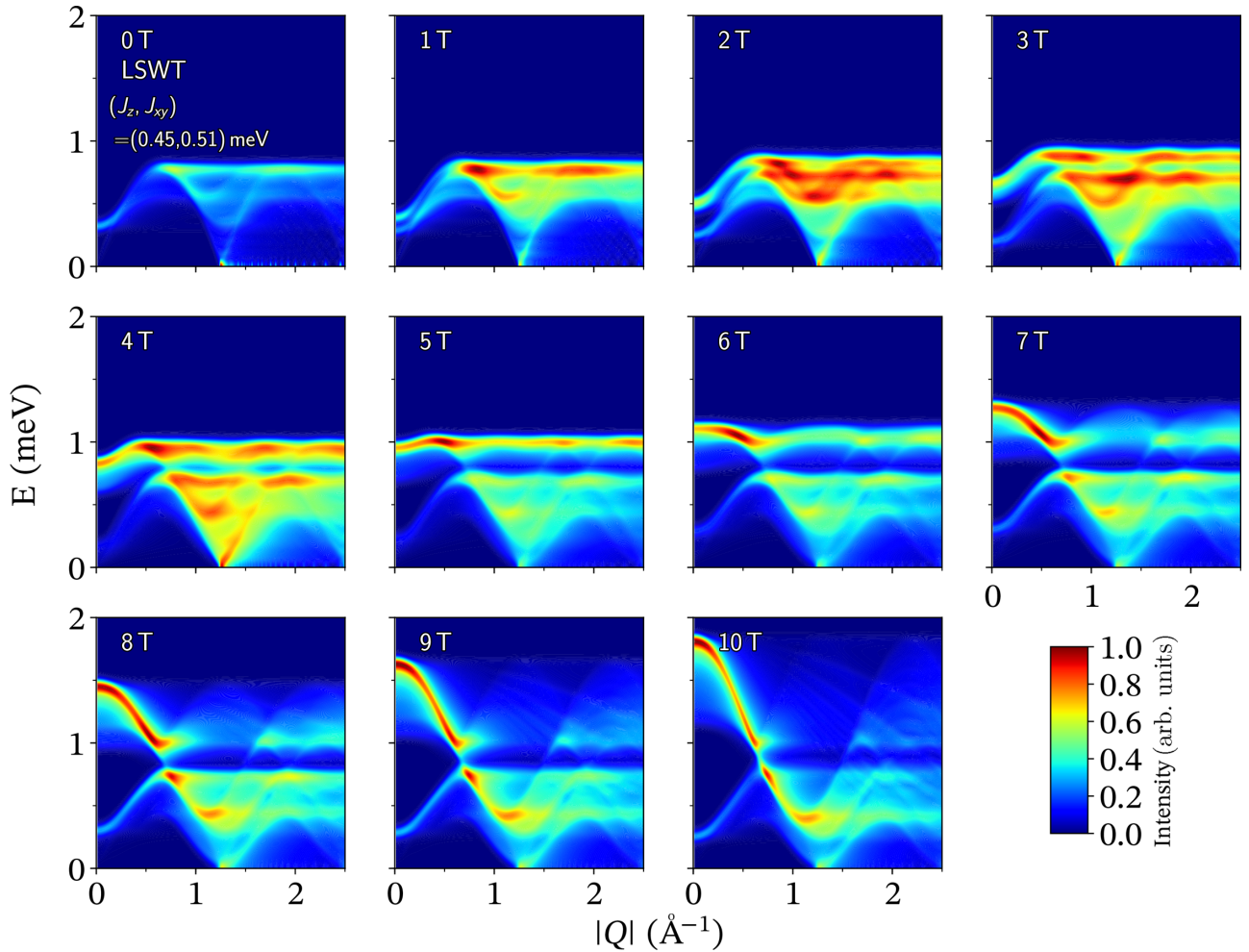


FIG. 8. Linear spin-wave theory (LSWT) calculations showing $S(Q, \hbar\omega)$ as a function of field for powder-averaged Yb^{3+} ions on a two-dimensional triangular lattice assuming three-sublattice ordering derived from the proposed spin model for NaYbO_2 [54]. At 0 T, NaYbO_2 does not show magnetic ordering, and therefore LSWT fails to capture the continuum of excitations from the quantum disordered ground state.

their critical field and become gapped, and at $B \sim 21$ T the last gapless configuration (corresponding to a perpendicular field) vanishes, leaving behind a fully gapped low-energy intensity.

2. Region 2

A flat intensity region is discernible at fields smaller than ≈ 6 T. At zero field, the flat intensity appears at energy $E \sim 0.8$ meV; as field increases, the flat region starts to split and form two flat regions, one moving towards higher energy and the other towards lower energy. The higher-energy flat region approaches $E \sim 1.0$ meV at $B = 5$ T, which corresponds to the observed flat intensity in neutron-scattering experiments at the same field strength. As the field further increases, the higher and lower-energy flat intensities vanish at $B \sim 6.5$ and ~ 8.5 T, respectively.

3. Region 3

The behavior of the intensities at zero momentum $|Q| \sim 0$ changes drastically as the field is varied. When the field is small, the zero momentum intensity is weak and at low energy, resulting in a visual downturn from the higher-energy flat intensities. As the field increases, the zero momentum

intensity also increases and moves towards higher energies; the downturn finally vanishes at $B = 5.5$ T, resulting in a globally flat intensity across all the plotted momenta. Further increasing the field will result in an upturn of the zero momentum intensity, meaning the zero momentum intensity further increases and becomes the highest energy intensity in the plot. The evolution of the zero momentum intensity is closely related to the large in-plane component of the field [54]; after the field exceeds the in-plane critical field $B_{xy,c}$, the configuration with an in-plane field has a gapped spin-wave spectrum, which is responsible for the highly dispersed, high intensity branch of the plot.

V. DISCUSSION

Crystalline electric-field calculations allow for the determination of characteristics of Yb ions in the single-ion limit. The two proposed fits for NaYbO_2 shown in Table I and Fig. 2 are qualitatively comparable. Although the first fit does not have a physical point-charge basis, it better represents the observed INS data, g -tensor components in Table I, as well as the observed moment size of $1.36(1) \mu_B$ in the 5-T magnetically ordered up-up-down phase [54]. Discrepancies

between this model and that recently reported by Ding *et al.* [53] likely arise from the way the susceptibility was treated in modeling the data. In the present case, susceptibility data in Fig. 2(b) were modeled by incorporating the large θ_{CW} field of NaYbO₂ [54] rather than fitting the high-temperature part of the susceptibility, absent exchange.

Within the higher incident energy INS data in Fig. 2, excitations out of the CEF ground state do not show resolvable broadening effects from chemical disorder [41,67], and all intramultiplet excitations can be indexed. Site mixing changes to CEF excitations can be roughly parametrized via the point-charge model shown in Eq. (5), and in Table S1 of Supplemental Material [70] varying degrees of chemical site mixing are shown incorporated out to the second shell of ions. At this distance, the smallest energy shift of a CEF excitation due to disorder in Table S1 is more than 4 meV, and the disordered CEF doublet energies do not shift equally under site disorder. Resolving these shifts and any resulting energy broadening are accessible with the instrumental resolution of the $E_i = 150$ meV data, and the absence of broadening in the data constrains any innate chemical disorder in NaYbO₂ to be weak. While unresolved local disorder can split CEF levels in certain scenarios and its influence cannot be completely excluded in our present data, prior analysis of the average structure of NaYbO₂ does not resolve the necessary disorder.

Instead, the subtle peak splitting observed in the first excited doublet in the higher resolution $E_i = 60$ meV of Fig. 3 likely arises from substantial exchange between Yb ions in NaYbO₂. Yb ions reside only ≈ 3.35 Å apart in NaYbO₂, and f -orbital overlap can induce CEF dispersion as is commonly found in closely spaced nondilute Ln-ion materials [67,76]. This effect is not visible in the $E_i = 150$ meV data as the instrumental resolution at that energy transfer exceeds the observed splitting of ≈ 2.1 meV for all CEF excitations (Fig. 1). A strong exchange-induced splitting in the powder-averaged mode energies is consistent with the calculated susceptibilities for the CEF fits in Fig. 2 only coinciding with raw NaYbO₂ data if the previously determined $\theta_{CW} = -10.3$ K [54] is implemented. For reference, compared with the other Yb-based materials, $|\theta_{CW}|$ is more than two times larger than YbMgGaO₄ ($|\theta_{CW}| = 4$ K) [38–44] and an order of magnitude larger than Yb₂Ti₂O₇ ($|\theta_{CW}| = 0.4$ K) [67,77–79].

At lower energies, the zero-field INS spectrum shows a diffuse continuum of excitations roughly centered about the $\mathbf{Q} = (1/3, 1/3, 0)$ position and emblematic of excitations within a highly frustrated, quantum disordered state [53,54]. This continuum has a bandwidth of approximately 1 meV, and it sharply contrasts the expectations of coherent, dispersive modes from spin-wave analysis of a low-temperature 120° ordered state (Fig. 8). Spectral weight at the K point $\mathbf{Q} = (1/3, 1/3, 0)$ is present down to the lowest energies resolved, $E = 0.1$ meV; however, a peak appears in the spectral weight of the continuum at $E = 0.25$ meV. This suggests that part of the spectrum is gapped, for instance, through damped magnons mixed within the continuum [71], or that this feature is inherent to the structure factor of the continuum itself.

With increasing field, the ground-state degeneracy is lifted and NaYbO₂ enters the classically understood, ordered regime. By 2.75 T, evidence for the ordered up-up-down phase appears as the spin liquid phase recedes, and the INS data

develop a powder-averaged flat band that increases in energy with increasing field. This tracks spin-wave predictions for the canted up-up-down phase in Fig. 8. While this band is pushed up, another powder-averaged low-energy band appears pushed downward toward zero energy near the previously reported high-field phase boundary [54]. The mode softening at this upper-field boundary may indicate the appearance of another, nearby magnetically ordered state prior to entering the quantum paramagnetic regime. Previous NMR studies have suggested such a boundary exists [56], and numerical cluster mean-field methods predict a first-order boundary into a neighboring V state near 70% of the saturation field [74]. The interpolated mode softening occurs near $H \approx 9.5$ T, which is consistent with the $H_{\text{sat}} \approx 14$ T for NaYbO₂ [53,54,56].

Further supporting the presence of a first-order high-field phase boundary in NaYbO₂, neutron-diffraction data plotted in Fig. 6 demonstrate an irreversibility in spin correlations that arises upon crossing into the ordered state from the low-versus the high-field boundaries. The nature of this phase boundary merits further investigation, and it does not appear in the 2D classical phase diagram plotted in Fig. 7. This suggests it likely derives from interplane coupling terms, consistent with predictions of numerical mean-field models [74]. While the collinear up-up-down state emerges upon crossing into the ordered regime from below, the appearance of the previously absent $\mathbf{Q} = (1/3, 1/3, 2)$ peak upon entering the ordered regime from above implies a more noncollinear phase, consistent with a V phase although single-crystal measurements are required to fully unravel the nature of this hysteretic transition.

Another feature that merits further study with single crystals is the appearance of resolvable magnetic scattering above the single-magnon cutoff in the up-up-down state. The ability to resolve a broad band of scattering near 1.5 meV at $E^* \approx 3J$ suggests substantial magnon-magnon interactions and spectral weight transferred into the multimagnon sector of the INS spectrum [72,73]. This would be consistent with presence of strong quantum fluctuations responsible for the reduction of the ordered moment and for transferring scattering weight into longitudinal spin fluctuations. Earlier single-crystal measurements of the up-up-down state of Ba₃CoSb₂O₉ failed to identify similar scattering [72], but quantum fluctuations are likely substantially enhanced in NaYbO₂ due to its strong interlayer frustration.

In fact, the *ABC* stacking sequence of layers in NaYbO₂ is frustrated relative to the *AAA* stacking in Ba₃CoSb₂O₉ and related materials [72,80–85]. Unfrustrated bonds between layers are generated when ions reside directly above each other (*AAA*), while frustration with three equivalent bonds forms when ions projected onto neighboring sheets reside at the centers of the triangular lattice. For instance, simulations of Ising moments on triangular lattice antiferromagnets with *ABC* and *ABAB* stacking have indeed shown that the frustrating interlayer interaction pushes magnetic ordering lower in temperature in comparison to *AAA* stacking [86]. Remarkably, due to its structure type promoting strong in-plane and interplane frustration, NaYbO₂ is joined by a host of *ALnX₂* compounds to emerge in recent literature [53–61] with seemingly quantum disordered magnetic ground states. For instance, both NaYbS₂ [61–63] and NaYbSe₂ [60] have

been proposed to display quantum spin liquid ground states. Other Ln species such as Ce [58] and Er [57] have also been investigated within this lattice type as potential hosts of quantum disordered magnetic states. This suggests a rich realm of materials for exploring the XXZ Hamiltonian in Eq. (6)—one in which $ALnQ_2$ compounds of varying local character can be used to explore the potential unconventional states predicted at this frontier.

VI. CONCLUSIONS

$NaYbO_2$ stands as a chemically ideal quantum spin liquid candidate stabilized on an equilateral triangular lattice. The intramultiplet structure and CEF ground-state doublet of Yb^{3+} ions in $NaYbO_2$ composed of mixed $|\pm 1/2\rangle$, $|\pm 5/2\rangle$, and $|\pm 7/2\rangle$ states were identified via high-energy inelastic neutron-scattering measurements. A subtle peak splitting is identified in the ground state's excitation spectrum that cannot be explained by trivial disorder and is, instead, consistent with weak CEF dispersion due to Yb exchange in this compound. The evolution of the low-energy inelastic spectra of $NaYbO_2$ is also reported. While low-temperature zero-field powder-averaged data reveal a weighted continuum of excitations without magnetic order or spin freezing, upon increasing field, the spectra evolve into that predicted for an up-up-down magnetically ordered phase. At the high-field phase boundary of the ordered state, a field-hysteretic diffraction pattern appears

and suggests a first-order phase boundary into a noncollinear state. Indications of strong magnon-magnon interactions are shown through the observation of appreciable spectral weight in the multimagnon spectrum of the field-induced ordered state. Future neutron-scattering experiments on single-crystal specimens of $NaYbO_2$ and related compounds are highly desired to resolve the detailed phase boundaries and higher-order spin dynamics of the field-stabilized order.

ACKNOWLEDGMENTS

This work was supported by the US Department of Energy (DOE), Office of Basic Energy Sciences, Division of Materials Sciences and Engineering under Grant No. DE-SC0017752 (S.D.W. and M.B.). M.B. acknowledges partial support by the National Science Foundation Graduate Research Fellowship Program under Grant No. 1650114. Work by L.B. and C.L. was supported by the DOE, Office of Science, Basic Energy Sciences under Grant No. DE-FG02-08ER46524. P.M.S. acknowledges financial support from the California Nanosystems Institute at University of California, Santa Barbara, through the Elings Fellowship. Identification of commercial equipment does not imply recommendation or endorsement by NIST. A portion of this research used resources at the Spallation Neutron Source, a DOE Office of Science User Facility operated by the Oak Ridge National Laboratory.

-
- [1] P. W. Anderson, *Mater. Res. Bull.* **8**, 153 (1973).
 - [2] P. W. Anderson, *Science* **235**, 1196 (1987).
 - [3] L. Balents, *Nature (London)* **464**, 199 (2010).
 - [4] L. Savary and L. Balents, *Rep. Prog. Phys.* **80**, 016502 (2016).
 - [5] P. A. Lee, *Science* **321**, 1306 (2008).
 - [6] W. Witczak-Krempa, G. Chen, Y. B. Kim, and L. Balents, *Annu. Rev. Condens. Matter Phys.* **5**, 57 (2014).
 - [7] Y. Zhou, K. Kanoda, and T.-K. Ng, *Rev. Mod. Phys.* **89**, 025003 (2017).
 - [8] C. Broholm, R. Cava, S. Kivelson, D. Nocera, M. Norman, and T. Senthil, *Science* **367**, 263 (2020).
 - [9] B. Bernu, C. Lhuillier, and L. Pierre, *Phys. Rev. Lett.* **69**, 2590 (1992).
 - [10] L. Capriotti, A. E. Trumper, and S. Sorella, *Phys. Rev. Lett.* **82**, 3899 (1999).
 - [11] R. Moessner and S. L. Sondhi, *Phys. Rev. Lett.* **86**, 1881 (2001).
 - [12] G. Jackeli and D. A. Ivanov, *Phys. Rev. B* **76**, 132407 (2007).
 - [13] S. Furukawa and G. Misguich, *Phys. Rev. B* **75**, 214407 (2007).
 - [14] A. Ralko, M. Ferrero, F. Becca, D. Ivanov, and F. Mila, *Phys. Rev. B* **71**, 224109 (2005).
 - [15] Y.-D. Li, X. Wang, and G. Chen, *Phys. Rev. B* **94**, 035107 (2016).
 - [16] L. O. Manuel and H. A. Ceccatto, *Phys. Rev. B* **60**, 9489 (1999).
 - [17] T. Jolicoeur, E. Dagotto, E. Gagliano, and S. Bacci, *Phys. Rev. B* **42**, 4800 (1990).
 - [18] W.-J. Hu, S.-S. Gong, W. Zhu, and D. N. Sheng, *Phys. Rev. B* **92**, 140403(R) (2015).
 - [19] Z. Zhu and S. R. White, *Phys. Rev. B* **92**, 041105(R) (2015).
 - [20] Y. Iqbal, W.-J. Hu, R. Thomale, D. Poilblanc, and F. Becca, *Phys. Rev. B* **93**, 144411 (2016).
 - [21] G. Misguich, C. Lhuillier, B. Bernu, and C. Waldtmann, *Phys. Rev. B* **60**, 1064 (1999).
 - [22] R. V. Mishmash, J. R. Garrison, S. Bieri, and C. Xu, *Phys. Rev. Lett.* **111**, 157203 (2013).
 - [23] A. Wietek and A. M. Läuchli, *Phys. Rev. B* **95**, 035141 (2017).
 - [24] H. F. Pen, J. van den Brink, D. I. Khomskii, and G. A. Sawatzky, *Phys. Rev. Lett.* **78**, 1323 (1997).
 - [25] T. M. McQueen, P. W. Stephens, Q. Huang, T. Klimczuk, F. Ronning, and R. J. Cava, *Phys. Rev. Lett.* **101**, 166402 (2008).
 - [26] D. Khomskii and M. Mostovoy, *J. Phys. A: Math. Gen.* **36**, 9197 (2003).
 - [27] M. V. Mostovoy and D. I. Khomskii, *Phys. Rev. Lett.* **89**, 227203 (2002).
 - [28] M. Giot, L. C. Chapon, J. Androulakis, M. A. Green, P. G. Radaelli, and A. Lappas, *Phys. Rev. Lett.* **99**, 247211 (2007).
 - [29] R. Coldea, D. Tennant, R. Cowley, D. McMorro, B. Dorner, and Z. Tylczynski, *J. Phys.: Condens. Matter* **8**, 7473 (1996).
 - [30] N. van Well, O. Zaharko, B. Delley, M. Skoulatos, R. Georgii, S. van Smaalen, and C. Rüegg, *Ann. Phys. (NY)* **530**, 1800270 (2018).
 - [31] T. Ono, H. Tanaka, O. Kolomiyets, H. Mitamura, T. Goto, K. Nakajima, A. Oosawa, Y. Koike, K. Kakurai, J. Klenke *et al.*, *J. Phys.: Condens. Matter* **16**, S773 (2004).

- [32] J. Alicea and M. P. A. Fisher, *Phys. Rev. B* **75**, 144411 (2007).
- [33] X. Zhang, F. Mahmood, M. Daum, Z. Dun, J. A. M. Paddison, N. J. Laurita, T. Hong, H. Zhou, N. P. Armitage, and M. Mourigal, *Phys. Rev. X* **8**, 031001 (2018).
- [34] Q. Sheng and C. L. Henley, *J. Phys.: Condens. Matter* **4**, 2937 (1992).
- [35] I. Kimchi, A. Nahum, and T. Senthil, *Phys. Rev. X* **8**, 031028 (2018).
- [36] Z. Zhu, P. A. Maksimov, S. R. White, and A. L. Chernyshev, *Phys. Rev. Lett.* **119**, 157201 (2017).
- [37] Y.-D. Li, Y. Shen, Y. Li, J. Zhao, and G. Chen, *Phys. Rev. B* **97**, 125105 (2018).
- [38] Y. Li, D. Adroja, P. K. Biswas, P. J. Baker, Q. Zhang, J. Liu, A. A. Tsirlin, P. Gegenwart, and Q. Zhang, *Phys. Rev. Lett.* **117**, 097201 (2016).
- [39] Y. Li, G. Chen, W. Tong, L. Pi, J. Liu, Z. Yang, X. Wang, and Q. Zhang, *Phys. Rev. Lett.* **115**, 167203 (2015).
- [40] Y. Li, H. Liao, Z. Zhang, S. Li, F. Jin, L. Ling, L. Zhang, Y. Zou, L. Pi, Z. Yang *et al.*, *Sci. Rep.* **5**, 16419 (2015).
- [41] Y. Li, D. Adroja, R. I. Bewley, D. Voneshen, A. A. Tsirlin, P. Gegenwart, and Q. Zhang, *Phys. Rev. Lett.* **118**, 107202 (2017).
- [42] J. A. Paddison, M. Daum, Z. Dun, G. Ehlers, Y. Liu, M. B. Stone, H. Zhou, and M. Mourigal, *Nat. Phys.* **13**, 117 (2017).
- [43] Y.-D. Shen, Yaoand Li, H. Wo, Y. Li, S. Shen, B. Pan, Q. Wang, H. C. Walker, P. Steffens, M. Boehm, Y. Hao, D. L. Quintero-Castro, L. W. Harriger, M. D. Frontzek, L. Hao, S. Meng, Q. Zhang, G. Chen, and J. Zhao, *Nature (London)* **540**, 559 (2016).
- [44] Y. Xu, J. Zhang, Y. S. Li, Y. J. Yu, X. C. Hong, Q. M. Zhang, and S. Y. Li, *Phys. Rev. Lett.* **117**, 267202 (2016).
- [45] Y. Li, S. Bachus, H. Deng, W. Schmidt, H. Thoma, V. Hutanu, Y. Tokiwa, A. A. Tsirlin, and P. Gegenwart, *Phys. Rev. X* **10**, 011007 (2020).
- [46] F. A. Cevallos, K. Stolze, T. Kong, and R. Cava, *Mater. Res. Bull.* **105**, 154 (2018).
- [47] Y. Shen, C. Liu, Y. Qin, S. Shen, Y.-D. Li, R. Bewley, A. Schneidewind, G. Chen, and J. Zhao, *Nat. Commun.* **10**, 4530 (2019).
- [48] P. A. Maksimov, Z. Zhu, S. R. White, and A. L. Chernyshev, *Phys. Rev. X* **9**, 021017 (2019).
- [49] Z. Ma, J. Wang, Z.-Y. Dong, J. Zhang, S. Li, S.-H. Zheng, Y. Yu, W. Wang, L. Che, K. Ran, S. Bao, Z. Cai, P. Čermák, A. Schneidewind, S. Yano, J. S. Gardner, X. Lu, S.-L. Yu, J.-M. Liu, S. Li, J.-X. Li, and J. Wen, *Phys. Rev. Lett.* **120**, 087201 (2018).
- [50] Y. Li, *Adv. Quantum Technol.* **2**, 1900089 (2019).
- [51] Y. Li, S. Bachus, B. Liu, I. Radelytskyi, A. Bertin, A. Schneidewind, Y. Tokiwa, A. A. Tsirlin, and P. Gegenwart, *Phys. Rev. Lett.* **122**, 137201 (2019).
- [52] Y. Li, D. Adroja, D. Voneshen, R. I. Bewley, Q. Zhang, A. A. Tsirlin, and P. Gegenwart, *Nat. Commun.* **8**, 15814 (2017).
- [53] L. Ding, P. Manuel, S. Bachus, F. Grubler, P. Gegenwart, J. Singleton, R. D. Johnson, H. C. Walker, D. T. Adroja, A. D. Hillier, and A. A. Tsirlin, *Phys. Rev. B* **100**, 144432 (2019).
- [54] M. M. Bordelon, E. Kenney, C. Liu, T. Hogan, L. Posthuma, M. Kavand, Y. Lyu, M. Sherwin, N. P. Butch, C. Brown *et al.*, *Nat. Phys.* **15**, 1058 (2019).
- [55] W. Liu, Z. Zhang, J. Ji, Y. Liu, J. Li, X. Wang, H. Lei, G. Chen, and Q. Zhang, *Chin. Phys. Lett.* **35**, 117501 (2018).
- [56] K. M. Ranjith, D. Dmytriieva, S. Khim, J. Sichelschmidt, S. Luther, D. Ehlers, H. Yasuoka, J. Wosnitza, A. A. Tsirlin, H. Kühne, and M. Baenitz, *Phys. Rev. B* **99**, 180401(R) (2019).
- [57] J. Xing, L. D. Sanjeeva, J. Kim, W. R. Meier, A. F. May, Q. Zheng, R. Custelcean, G. R. Stewart, and A. S. Sefat, *Phys. Rev. Mater.* **3**, 114413 (2019).
- [58] J. Xing, L. D. Sanjeeva, J. Kim, G. R. Stewart, M.-H. Du, F. A. Reboredo, R. Custelcean, and A. S. Sefat, *ACS Mater. Lett.* **2**, 71 (2020).
- [59] J. Xing, L. D. Sanjeeva, J. Kim, G. R. Stewart, A. Podlesnyak, and A. S. Sefat, *Phys. Rev. B* **100**, 220407(R) (2019).
- [60] K. M. Ranjith, S. Luther, T. Reimann, B. Schmidt, P. Schlender, J. Sichelschmidt, H. Yasuoka, A. M. Strydom, Y. Skourski, J. Wosnitza, H. Kühne, T. Doert, and M. Baenitz, *Phys. Rev. B* **100**, 224417 (2019).
- [61] R. Sarkar, P. Schlender, V. Grinenko, E. Haeussler, P. J. Baker, T. Doert, and H.-H. Klauss, *Phys. Rev. B* **100**, 241116(R) (2019).
- [62] J. Sichelschmidt, P. Schlender, B. Schmidt, M. Baenitz, and T. Doert, *J. Phys.: Condens. Matter* **31**, 205601 (2019).
- [63] M. Baenitz, P. Schlender, J. Sichelschmidt, Y. A. Onykieenko, Z. Zangeneh, K. M. Ranjith, R. Sarkar, L. Hozoi, H. C. Walker, J.-C. Orain, H. Yasuoka, J. van den Brink, H. H. Klauss, D. S. Inosov, and T. Doert, *Phys. Rev. B* **98**, 220409(R) (2018).
- [64] K. Stevens, *Proc. Phys. Soc. London, Sect. A* **65**, 209 (1952).
- [65] O. Arnold, J.-C. Bilheux, J. Borreguero, A. Buts, S. I. Campbell, L. Chapon, M. Doucet, N. Draper, R. F. Leal, M. Gigg *et al.*, *Nucl. Instrum. Methods Phys. Res. Sec. A* **764**, 156 (2014).
- [66] A. Boothroyd, Spectre—A program for calculating spectroscopic properties of rare earth ions in crystals (1990), <https://xray.physics.ox.ac.uk/software.htm>.
- [67] J. Gaudet, D. D. Maharaj, G. Sala, E. Kermarrec, K. A. Ross, H. A. Dabkowska, A. I. Kolesnikov, G. E. Granroth, and B. D. Gaulin, *Phys. Rev. B* **92**, 134420 (2015).
- [68] Z. Zangeneh, S. Avdoshenko, J. van den Brink, and L. Hozoi, *Phys. Rev. B* **100**, 174436 (2019).
- [69] I. Sumarlin, J. Lynn, T. Chattopadhyay, S. Barilo, and D. Zhigunov, *Physica C* **219**, 195 (1994).
- [70] See Supplemental Material at <http://link.aps.org/supplemental/10.1103/PhysRevB.101.224427> for further experimental details on spin-wave spectra and crystalline electric-field excitations.
- [71] F. Ferrari and F. Becca, *Phys. Rev. X* **9**, 031026 (2019).
- [72] Y. Kamiya, L. Ge, T. Hong, Y. Qiu, D. Quintero-Castro, Z. Lu, H. Cao, M. Matsuda, E. Choi, C. Batista *et al.*, *Nat. Commun.* **9**, 1 (2018).
- [73] M. Mourigal, W. T. Fuhrman, A. L. Chernyshev, and M. E. Zhitomirsky, *Phys. Rev. B* **88**, 094407 (2013).
- [74] D. Yamamoto, G. Marmorini, and I. Danshita, *Phys. Rev. Lett.* **114**, 027201 (2015).
- [75] S. Miyashita, *J. Phys. Soc. Jpn.* **55**, 3605 (1986).
- [76] P. Fulde and M. Loewenhaupt, *Adv. Phys.* **34**, 589 (1985).
- [77] S. Bramwell, M. Field, M. Harris, and I. Parkin, *J. Phys.: Condens. Matter* **12**, 483 (2000).
- [78] J. Hodges, P. Bonville, A. Forget, M. Rams, K. Królas, and G. Dhalenne, *J. Phys.: Condens. Matter* **13**, 9301 (2001).
- [79] R. M. D’Ortenzio, H. A. Dabkowska, S. R. Dunsiger, B. D. Gaulin, M. J. P. Gingras, T. Goko, J. B. Kycia, L. Liu, T. Medina, T. J. Munsie, D. Pomaranski, K. A. Ross, Y. J. Uemura, T. J. Williams, and G. M. Luke, *Phys. Rev. B* **88**, 134428 (2013).

- [80] J. Ma, Y. Kamiya, T. Hong, H. B. Cao, G. Ehlers, W. Tian, C. D. Batista, Z. L. Dun, H. D. Zhou, and M. Matsuda, *Phys. Rev. Lett.* **116**, 087201 (2016).
- [81] R. Rawl, L. Ge, H. Agrawal, Y. Kamiya, C. R. Dela Cruz, N. P. Butch, X. F. Sun, M. Lee, E. S. Choi, J. Oitmaa, C. D. Batista, M. Mourigal, H. D. Zhou, and J. Ma, *Phys. Rev. B* **95**, 060412(R) (2017).
- [82] Y. Cui, J. Dai, P. Zhou, P. S. Wang, T. R. Li, W. H. Song, J. C. Wang, L. Ma, Z. Zhang, S. Y. Li, G. M. Luke, B. Normand, T. Xiang, and W. Yu, *Phys. Rev. Mater.* **2**, 044403 (2018).
- [83] Y. Kojima, M. Watanabe, N. Kurita, H. Tanaka, A. Matsuo, K. Kindo, and M. Avdeev, *Phys. Rev. B* **98**, 174406 (2018).
- [84] G. Koutroulakis, T. Zhou, Y. Kamiya, J. D. Thompson, H. D. Zhou, C. D. Batista, and S. E. Brown, *Phys. Rev. B* **91**, 024410 (2015).
- [85] Y. Shirata, H. Tanaka, A. Matsuo, and K. Kindo, *Phys. Rev. Lett.* **108**, 057205 (2012).
- [86] D. T. Liu, F. J. Burnell, L. D. C. Jaubert, and J. T. Chalker, *Phys. Rev. B* **94**, 224413 (2016).